9-15-2023

Constraints on Near-Ridge Magmatism Using $^{40}Ar/^{39}Ar$ Geochronology of Enriched MORB from the 8°20' N Seamount Chain

Molly K. Anderson
University of Florida

Michael R. Perfit
University of Florida

Leah E. Morgan
United States Geological Survey

Daniel J. Fornari
Woods Hole Oceanographic Institution

Michael Cosca
United States Geological Survey

See next page for additional authors

Publication Information

Anderson, Molly K.; Perfit, Michael R.; Morgan, Leah E.; Fornari, Daniel J.; Cosca, Michael; and Wanless, V. Dorsey. (2023). "Constraints on Near-Ridge Magmatism Using $^{40}Ar/^{39}Ar$ Geochronology of Enriched MORB from the 8°20' N Seamount Chain". *Earth and Planetary Science Letters, 618*, 118278.
https://doi.org/10.1016/j.epsl.2023.118278

Molly K. Anderson, Michael R. Perfit, Leah E. Morgan, Daniel J. Fornari, Michael Cosca, and V. Dorsey Wanless

Earth and Planetary Science Letters 618 (2023) 118278

Contents lists available at ScienceDirect

Earth and Planetary Science Letters

journal homepage: www.elsevier.com/locate/epsl

Constraints on near-ridge magmatism using $^{40}Ar/^{39}Ar$ geochronology of enriched MORB from the 8°20' N seamount chain

Molly K. Anderson[a,*], Michael R. Perfit[a], Leah E. Morgan[b], Daniel J. Fornari[c], Michael Cosca[b], V. Dorsey Wanless[d]

[a] *Department of Geological Sciences, University of Florida, Gainesville, FL 32611, United States of America*
[b] *United States Geological Survey, Geology, Geophysics, Geochemistry Science Center, Denver, CO 80225, United States of America*
[c] *Department of Geology and Geophysics, Woods Hole Oceanographic Institution, Woods Hole, MA 02543, United States of America*
[d] *Department of Geosciences, Boise State University, Boise, ID 83725, United States of America*

ARTICLE INFO

Article history:
Received 5 December 2022
Received in revised form 6 June 2023
Accepted 12 June 2023
Available online xxxx
Editor: L. Coogan

Dataset link: https://doi.org/10.5066/P9ECGKYO

Dataset link: https://doi.org/10.26022/IEDA/111616

Keywords:
off-axis MORB magmatism
Ar/Ar geochronology
mantle heterogeneity
East Pacific Rise
dating young MORB

ABSTRACT

Our understanding of the spatial-temporal-compositional relationships between off-axis magmatism and mid-ocean ridge spreading centers is limited. Determining the $^{40}Ar/^{39}Ar$ ages of mid-ocean ridge basalt (MORB) lavas erupting near mid-ocean ridges (MOR) has been a challenge due to the characteristically low K_2O contents in incompatible element-depleted normal MORB (NMORB). High-precision $^{40}Ar/^{39}Ar$ geochronology is used here to determine ages of young, basaltic lavas erupted along the 8°20' N seamount chain west of the East Pacific Rise (EPR) axis that have a range of incompatible element enrichments (EMORB) suitable for $^{40}Ar/^{39}Ar$ geochronology (e.g., K_2O contents $>$ 0.3 wt%). $^{40}Ar/^{39}Ar$ ages were determined in 29 well-characterized basalts sampled using HOV *Alvin* and dredging. Detailed geochronology and geochemical analyses provide important constraints on the timing, distribution, and origins of lavas that constructed this extensive volcanic lineament relative to magmatism beneath the adjacent EPR axis. Seamount eruption ages are up to ∼1.6 Ma younger than the underlying lithosphere, supporting a model of prolonged off-axis magmatism for at least 2 Myrs at distances as great as ∼90 km from the ridge axis. Increasing geochemical heterogeneity with eruption distance reflects the diminishing effect of sub-ridge melt focusing. The range of geochemically distinct lavas erupted at given distances from the ridge highlights the dynamic nature of the near-ridge magmatic environment over Myr timescales. Linear ridge-like (EPR-parallel) morphotectonic features erupt the youngest and most incompatible element-enriched lavas of the entire seamount chain, indicating there is a recent change in the influence of mantle heterogeneity and off-axis melt metasomatism on the near-ridge lithospheric mantle. Changes in seamount morphologies are attributed to counter-clockwise rotation and southward migration of the nearby Siqueiros transform over the last few million years.

1. Introduction

Seamounts ubiquitously form near mid-ocean ridges (MORs), but their origins and relationships to MOR magmatism remain largely unconstrained due to the generally sparse sampling of near-ridge seamounts and difficulty in determining ages of young, low-K_2O lavas. Geochemical studies of seamounts adjacent to the East Pacific Rise (EPR) crest show that seamount lavas have greater and more variable incompatible element abundances than typical normal MORB (NMORB) erupted at the ridge crest. Hence, near-ridge seamounts may provide key constraints on MOR mantle chemical heterogeneity and melting systematics that are commonly obscured in axial MORB lava geochemistry (Graham et al., 1988; Batiza et al., 1989; Niu and Batiza, 1997; Wendt et al., 1999; Kamenetsky and Maas, 2002; Niu et al., 2002; Husen et al., 2016; Mallick et al., 2019; Anderson et al., 2021). $^{40}Ar/^{39}Ar$ dating is critical for constraining spatial and temporal mantle and crustal MOR processes and is best applied to off-axis magmatic settings where EMORB are commonly recovered (Zindler et al., 1984; Niu and Batiza, 1997; Brandl et al., 2012; Gill et al., 2016). The incompatible element enriched compositions of many off-axis seamount lavas (EMORB; e.g., K/Ti ($K_2O/TiO_2\times100$) >16) are suitable for determining $^{40}Ar/^{39}Ar$ ages of intraplate and near-ridge magmatism. Historically, sampling has often been restricted to only a few sample sites per seamount, without detailed geological context for the sample location, and many samples have been collected from older

* Corresponding author.
E-mail address: mollyanderson@ufl.edu (M.K. Anderson).

https://doi.org/10.1016/j.epsl.2023.118278

seamounts distal to a MOR axis (Duncan, 1984; Honda et al., 1987; Koppers et al., 2000, 2001, 2003).

Numerous challenges are faced when dating young, incompatible element-depleted submarine basalts, complicating attempts to determine timing and systematics of off-axis magmatism. First, typical incompatible element-depleted NMORB possess few U, Th, and K-bearing mineral phases, a key requirement for Pb and Ar geochronology. Second, near-ridge lavas are geologically young, yielding insufficient time for potassium to decay to measurable amounts of radiogenic argon compared to trapped argon (Duncan and Hogan, 1994). Third, seafloor alteration processes may remove radiogenic argon particularly from volcanic glass, contaminate the glass with seawater potassium, and/or hydrothermally alter common mineral phases like plagioclase (Jiang et al., 2021). Fourth, exposure to atmospheric $^{40}Ar/^{36}Ar$ ratios during sample acquisition and processing can contaminate the sample and thus samples must be incrementally heated to remove these effects (Koppers et al., 2000; Graham, 2002). Fifth, rapid quenching of seafloor basalt lavas may also retain excess non-atmospheric, mantle-derived $^{40}Ar/^{36}Ar$, resulting in artificially old plateau ages from $^{40}Ar/^{39}Ar$ geochronology (Heaton and Koppers, 2019). As a result of these limitations, many studies of seamount lavas sampled near MOR crests have relied on relative dating – using visual estimates, magnetic polarity mapping or paleo-intensities (Bowles et al., 2006; Choi et al., 2021), and/or overlying sediment thicknesses (Batiza et al., 1989; Fabbrizzi et al., 2022). U-series disequilibria and Po-Pb dating have been important in studies of very young axial MORB eruptions, but are limited to eruption ages less than a few hundred thousand years (Rubin et al., 1994; Perfit and Chadwick, 1998; Sims et al., 2003; Rubin et al., 2005; Turner et al., 2011).

Most successful seafloor basalt ages acquired using $^{40}Ar/^{39}Ar$ geochronology focus on long-lived hotspot systems, and/or old off-axis seamounts. At these sites, more significant periods of time have elapsed since eruption, allowing for incompatible element-depleted lavas to produce sufficient radiogenic Ar for reliable measurements (Duncan, 1984; Desonie and Duncan, 1990; Koppers et al., 2001, 2003, 2004; Clouard and Bonneville, 2005; Clague et al., 2009; Heaton and Koppers, 2019). Few successful applications of $^{40}Ar/^{39}Ar$ geochronology have been applied to young MORB. Ages of off-axis lavas recovered west of 9°30' N and 11°20' N on the EPR, out to the Brunhes-Matuyama boundary (up to 1 Ma), revealed eruptive ages consistent with spreading rates (Duncan and Hogan, 1994). Only half of the attempted analyses were usable due to large amounts of atmospheric ^{40}Ar overwhelming radiogenic argon across all incremental heating steps (Duncan and Hogan, 1994). In another case, basalts from the Rano Rahi seamount field extending between the southern EPR and Pukapuka Ridge (~16° and 19° S) have also successfully been dated using high resolution incremental heating $^{40}Ar/^{39}Ar$ geochronology methods on dredged, geochemically heterogeneous basalts. The analyses provided evidence of near-ridge magmatism up to 60 km from the EPR ridge axis (Hall et al., 2006).

Prior to this study, no linear near-ridge seamount chains oriented perpendicular to a MOR have been dated using $^{40}Ar/^{39}Ar$ geochronology. Furthermore, there are very few studies combining closely spaced (a few km), in-situ sampling using submersibles combined with absolute dating to address small-scale spatial and temporal variability of the mantle in the near-ridge environment. The ~150 km long 8°20' N seamount chain, oriented perpendicular to the northern EPR, was deemed an ideal location for an $^{40}Ar/^{39}Ar$ geochronology study due to its linear spatial relationship with the ridge on age-progressive lithosphere north of the western Siqueiros fracture zone (Fig. 1; Pockalny et al., 1997). Lavas that created the seamounts have compositions spanning the entire geochemical range of basalts previously documented for northern EPR MORB, with distinct chemical differences on some seamounts at small spatial scales (< 1 km) (Anderson et al., 2021). Regardless of their position along the chain, the seamounts primarily consist of young-looking pillow flows that are typically surrounded by pockets of pelagic sediment and are thinly coated with manganese oxide. Lobate and sheet flows are only rarely present and no systematic relationships between flow types and their compositions have been identified. Observationally, it is difficult to distinguish the relative ages of the samples.

The K_2O contents of the EMORB from the seamounts range from 0.20 to 1.76 wt%, and 129 of them are candidates for $^{40}Ar/^{39}Ar$ geochronology ($K_2O \geq 0.4$ wt%; Fig. 1). Since there are little/no systematic variations in basalt compositions along-chain, precise eruption ages are needed to ascertain if there are any spatial and/or temporal systematics in processes or sources responsible for generating basalts with such highly heterogeneous compositions on such small scales. Here ages for 29 of the 8°20' N seamount chain EMORB lavas have been determined using $^{40}Ar/^{39}Ar$ geochronology. Coupled with the regional seafloor spreading rate, comparisons between seamount eruption ages and the underlying age-progressive lithosphere allow us to determine paleo-eruption distances from the EPR spreading axis, constrain the tectono-magmatic development of the chain, and evaluate temporal and spatial changes in EMORB petrogenesis in lithosphere extending ~90 km from the adjacent EPR axis.

2. Background

2.1. Geologic setting

The northern EPR spreads at a full rate of ~110 mm/yr between 8° and 11°N (DeMets et al., 2010), and is divided into multiple first- and lower-order segments by large-offset transform faults (Clipperton and Siqueiros), overlapping spreading centers (OSCs) and smaller deviations of axial linearity (DEVALS) (Langmuir et al., 1986; Carbotte and Macdonald, 1992; Macdonald et al., 1992). Near 8°20'N, the EPR is offset 140 km by the Siqueiros transform, which itself is a ~20 km-wide deformation zone currently containing four intra-transform spreading centers (ITSCs) and five strike-slip faults (Crane, 1976; Fornari et al., 1989). The ITSCs reflect a prolonged history of plate reorganization and the resulting southward migration of the Siqueiros transform over the past 3.6 Ma (Pockalny et al., 1997; Wolfson-Schwehr and Boettcher, 2019). West of the EPR axis, on the northern side of the Siqueiros fracture zone trace near 8°20'N, is a chain of volcanoes and constructional volcanic ridges consisting of coalesced seamounts (Scheirer and Macdonald, 1995), referred to as the 8°20'N seamount chain (Fig. 1). The presence of ITSCs in the Siqueiros transform (Fornari et al., 1989; Perfit et al., 1996; Gregg et al., 2009; Hebert and Montési, 2011; Wolfson-Schwehr and Boettcher, 2019), and the evolution and reorganization of the plate boundary in this area over the past few million years (Pockalny et al., 1997) have resulted in several generally east-west trending structural lineaments on the Cocos Plate that juxtapose the 8°20'N seamounts west of the EPR axis (Fig. 1). These features are probably relicts of the northern Siqueiros transform deformation zone and have formed as the transform migrated southward over the last 1–2 Myr (Pockalny et al., 1997; Gregg et al., 2009; Romano et al., 2022).

The 8°20' N seamount chain is a ~150 km long lineament of volcanic features oriented perpendicular to the EPR between the Clipperton and Siqueiros transforms on the Pacific Plate (Fig. 1). At a regional scale, the chain follows a relative plate motion trend of ~260°, a notable contrast to other seamount groups and chains which are aligned parallel to the absolute spreading trend of ~330° (e.g., Lamont seamounts; Fornari et al., 1988a, 1988b; Allan et al., 1989). The closest seamount to the EPR (Oscar) is ~ 30 km northwest of the western ridge-transform intersection (RTI) of the

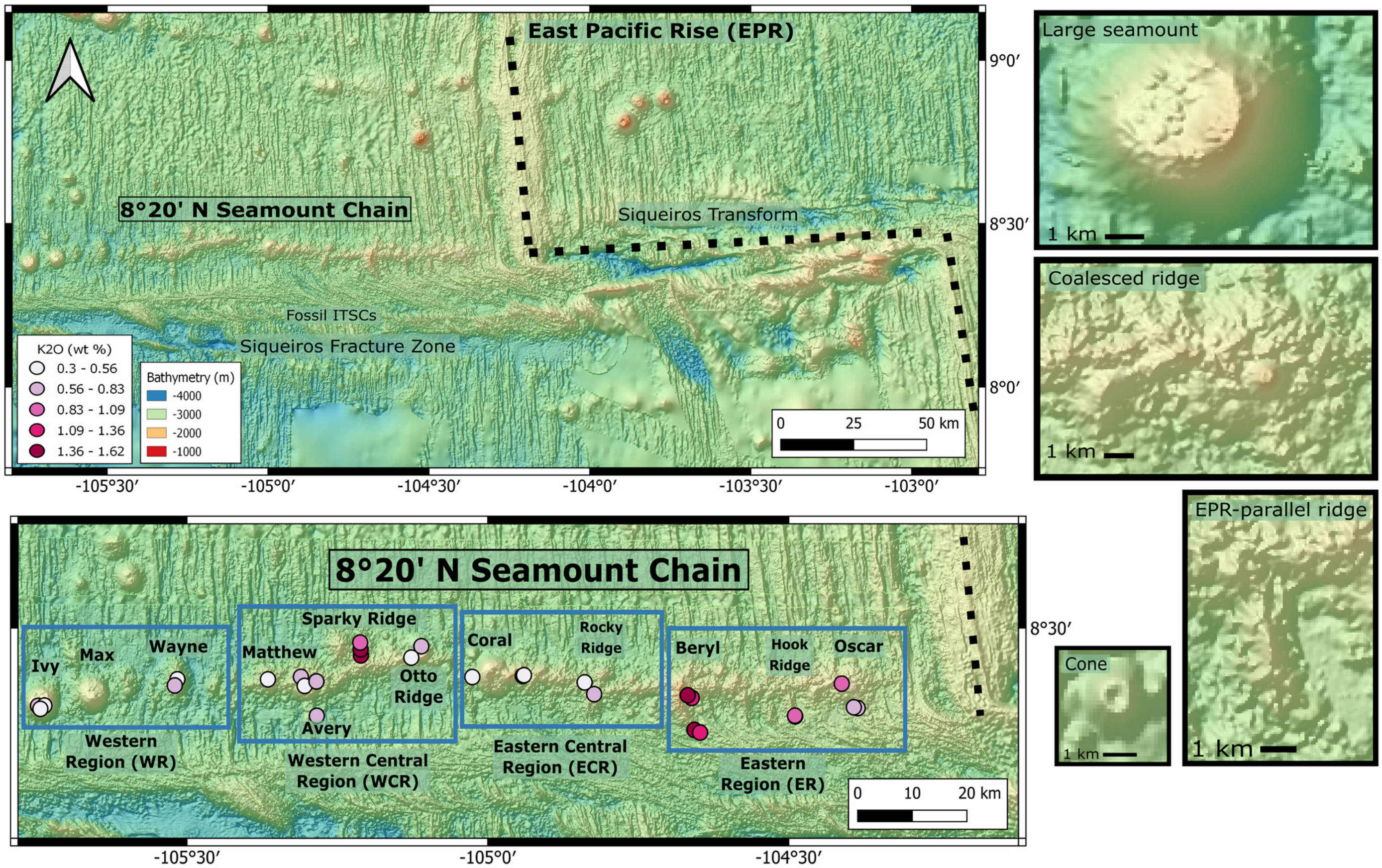

Fig. 1. Location of the 8°20' N seamount chain, the northern East Pacific Rise (EPR; black dashed line) and nearby Siqueiros transform fault. Maps are made from EM122 multibeam bathymetry acquired from AT37-05 expedition, gridded to 70-m node spacing, also showing the location of samples selected for $^{40}Ar/^{36}Ar$ dating along the span of the seamount chain. Blue boxes outline western region (WR), western central region (WCR), eastern central region (ECR), and eastern region (ER). Samples are represented by circles, with darkness of colors based on their respective K_2O (wt%) concentrations. Highest K_2O samples are darker pink whereas samples with depleted K_2O concentrations are lighter pink. Samples selected for argon dating covered both spatial and geochemical variability, although these analyses are limited to relatively high K_2O concentrations, and therefore only enriched MORB (EMORB) are represented in this study. The seamount chain consists of varied morphologies that change with decreasing lithospheric age (left to right). Examples of each morphology type are shown in the upper right. Prominent, large, round, and well-defined seamounts make up the western region of the chain (WR), emplaced over otherwise N-S trending abyssal hill fabric. The central portions of the chain consist of a mix of large, sub-rounded seamounts, N-S trending ridges, and E-W trending coalesced ridges (WCR and ECR). In the WCR, N-S trending ridges parallel to the EPR follow abyssal hills north of the chain (i.e., Sparky) and south of half of the chain up to Coral seamount. From Coral seamount and eastward (ECR), the abyssal hills south of the chain bend southeast toward the Siqueiros fracture zones, and a few of the sampled seamounts follow those EPR-parallel ridges (i.e. Beryl). The easternmost region (ER) consists of largely coalesced seamounts, also with N-S trending EPR-parallel ridges curving southwest toward the Siqueiros fracture zone (i.e., Hook Ridge and the southern flank of Oscar). The largest seamounts display calderas and breached calderas decorated with cones. South of the seamount chain are multiple E-W trending fracture zones and fossil intra-transform spreading centers (ITSCs) produced by the nearby, southward migrating, transtensional Siqueiros transform fault.

Siqueiros transform on ∼0.4 Ma lithosphere ∼ 20 km from the EPR axis. The chain extends westward on lithosphere up to ∼3.1 Ma (the current position of Ivy seamount) on the Pacific Plate. It consists of eleven named and several unnamed volcanic edifices with varying geometries based on their current position in the chain, their relative orientation, and seamount morphology (described in detail below).

2.2. 2016 and 2018 research expeditions

The first research expedition to the 8°20' N seamounts occurred in November 2016 on RV *Atlantis* (AT37-05). During this cruise the seamounts were mapped (using shipboard multibeam, gravity, and magnetics, and AUV Sentry near-bottom multibeam and sidescan). The geochemical and geophysical results are reported in Anderson et al. (2021) and Romano et al. (2022), respectively. A second research expedition in December 2018 on RV *Atlantis* (AT42-06) further sampled and mapped Oscar and Coral seamounts (Fig. 1), guided by geochemical data and maps resulting from the 2016 expedition. Combined, the research programs resulted in the collection of 328 basalts, 176 of which are enriched in incompatible elements (EMORB) relative to "normal" NMORB, and "depleted" DMORB (Anderson et al., 2021, 2022)

2.3. Morphological characterization of the seamounts

Segmentation of the 8°20' N seamount chain reflects long-term and/or large-scale changes in seamount morphological construction. To understand how these changes occur relative to the edifices' underlying lithosphere age, the seamounts are grouped into segments based on slight changes in lineament orientation, edifice shapes, and relationships between each seamount and the adjacent abyssal hill fabric (Fig. 1). The western region (WR) of the seamount chain is situated on the oldest lithosphere and is characterized by large, well-defined, circular seamounts (Ivy, Max, and Wayne) overprinted on the prominent N-S trending abyssal hill fabric (Fig. 1). Some of these large, well-defined seamounts (up to ∼8.6 km in diameter) contain craters and calderas, suggestive of prolonged magmatism associated with well-developed magma chambers and repeated episodes of magma supply, injection, and eruption over time (Fornari et al., 1984, 1988b; Clague et al., 2000).

Similarly, the western central region (WCR) of the seamount chain (Matthew, Avery, Sparky, and Otto Ridge) overlies N-S trending abyssal hill fabric, but this portion of the chain consists of large, partially coalesced, sub-circular edifices forming an ENE-WSW trending lineament. A significant amount of structural variability exists on this segment including: flat-topped 'pancake-like' structures south of Avery; large, rounded, caldera-bearing edifices; sub-circular seamounts like Matthew; N-S trending EPR-parallel ridges similar to Sparky; and E-W coalesced lineaments like Otto Ridge.

The eastern part of the chain, between the EPR and ~105°W, consists of continuous, ridge-like volcanic construct lineaments trending ~274° with partially-coalesced craters/calderas, some with small cones. The eastern central region (ECR) from Coral seamount to the west of Beryl seamount is a partially coalesced group of seamounts, oriented ESE-WNW with poorly defined edifices compared with seamounts from the western segments. Coral seamount is an exception, forming a large, circular seamount with a large caldera, flanked on both sides by E-W trending ridges. Another important change from Coral seamount eastward is the introduction of curvilinear EPR-parallel ridges south of the seamount chain that bend southeastward toward the Siqueiros transform-EPR intersection. Unlike the more typical, asymmetric, N-S trending abyssal hills of the western segments (Macdonald et al., 1996; Buck and Poliakov, 1998; Clague et al., 2000; Buck, 2001; Sohn and Sims, 2005), these eastern, curvilinear abyssal hills are symmetrically comprised of volcanic features (Fig. 2).

The eastern region (ER) of the seamount chain from Beryl to Oscar seamount consists of many N-S trending pillow mounds and ridges that coalesced into a larger E-W trending edifice. The N-S oriented ridges that follow abyssal hill fabric (north and south of the seamount chain) are referred to here as EPR-parallel ridges. Examples of these ridges are Sparky, Beryl, and Hook Ridge. These EPR-parallel ridges, extending southeastward of the main portion of the chain, consistently follow the curvilinear abyssal hill fabrics that bend into the Siqueiros fracture zone, similar to those observed in the ECR segment.

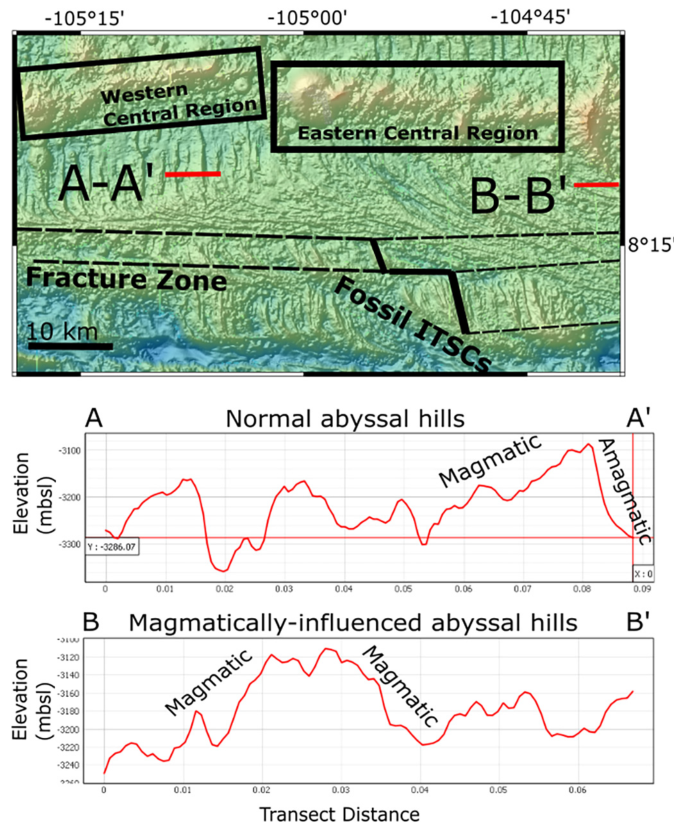

Fig. 2. Bathymetric map showing abyssal hill structures along two segments of the 8°20' N seamount chain (western central region and eastern central region). The normal abyssal hill structures (shown along transect A-A' south of western central region) are characterized by asymmetry such that ridge-facing flanks are amagmatic/tectonic and truncated compared to ridge-opposite facing flanks characterized by magmatism. These structures form in response to crustal stretching off-axis (Buck and Poliakov, 1998; Sohn and Sims, 2005). The magmatically influenced abyssal hill structures (shown along transect B-B' south of eastern central region) are more symmetrically formed from magmatism occurring on both ridge-facing and ridge-opposite facing flanks. This transition occurs between western central region and eastern central region, coincident with fossil intra-transform spreading centers (Pockalny et al., 1997) that have been abandoned by the southward migrating Siqueiros transform fault. Similar constructional features have been noted at RTI in other regions (Fox and Gallo, 1984; Phipps-Morgan and Parmentier, 1984).

3. Analytical methods and results

Twenty-nine aphyric, slightly to highly enriched EMORB whole rocks with K_2O abundances greater than 0.3 wt% (using a range of compositions where possible from each sampled seamount) were selected for $^{40}Ar/^{39}Ar$ geochronology along the full 150 km length of the 8°20' N seamount chain. After crushing, clean, alteration-free whole rock pieces < 3 mm in diameter were handpicked using a binocular microscope. Samples were rinsed in deionized water, then loaded in aluminum disks with the Fish Canyon sanidine neutron fluence monitor (Kuiper et al., 2008) and subsequently irradiated at the U.S. Geological Survey (USGS) TRIGA reactor in Denver, CO, converting ^{39}K to ^{39}Ar to enable assessment of both parent and daughter isotopes on the same sample aliquot. Irradiated samples and standards were analyzed using a Thermo Scientific ARGUS VI mass spectrometer at the USGS Argon Geochronology Laboratory in Denver, CO. Samples were step-heated in 7 – 15 increments, and the released gas was purified using SAES getters and a cryogenic trap. Argon isotopes were measured simultaneously by multicollection using four Faraday detectors and one ion counter, measured 1-3 times per sample, with blank measurements every 1 to 2 analyses. Final data, corrected for backgrounds, discrimination, and radioactive decay, are provided in Morgan (2023) and Table 1. Inverse isochron and plateau ages were calculated using MassSpec software v.7.91, assuming an age of 28.201 +/− 0.023 (1σ) Ma for the Fish Canyon sanidine standard (Kuiper et al., 2008). Inverse isochron ages were determined by removing any steps containing < 2% of total ^{39}Ar released to reduce bias (Morgan et al., 2009). Preferred ages were selected from inverse isochron and plateau ages based on the method that yielded the best mean square weighted deviation (MSWD; acceptable MSWD = 0.5 – 2.5) and probability (P-values; acceptable P-values = 0.2 – 0.8; Supplementary Table 1), following methods in Morgan et al. (2009). Rapid quenching of seafloor basalts can trap non-atmospheric argon during eruption, which can be identified using the inverse isochron y-intercept, shown in Fig. 3 (a,b). Inverse isochron ages were therefore preferred where possible since they do not require assuming an initial $^{40}Ar/^{36}Ar$ value at the time of quenching. However, where the inverse isochron yielded poor MSWD and/or P-values, plateau ages (assuming a trapped atmospheric $^{40}Ar/^{36}Ar$ value of 298.56 +/− 0.31; Lee et al., 2006) were assigned. To demonstrate that the overall results and interpretations are not significantly impacted by the choice of isochron or plateau age, the alternative selections for each run (where available) are shown as grey symbols correlating with the selected samples (Fig. 4).

As expected, samples with < 0.4 wt% K_2O yielded the least precise ages; for example, sample 4851_13 containing 0.3 wt% K_2O resulted in an interpreted age of 1.03 +/− 0.92 Ma while the most incompatible element-enriched sample 4853_11 (with 1.62 wt% K_2O) yielded an interpreted age of 0.224 +/− 0.008 Ma. Eruption ages of the EMORB range from 0.11 +/− 0.11 Ma (indistinguish-

Table 1
Preferred inverse isochron or plateau ages for samples from the 8°20' N seamount chain in order of increasing lithosphere age. Selections were made based on best MSWD (0.5 – 2.5) and P-values (0.2 – 0.8) (see Supplementary Table 1 for all inverse isochron and plateau ages with these statistics). Isochron calculations do not include steps containing <2% total ^{39}Ar released. Errors are reported in 2-sigma. Eruption distances are calculated assuming 55 mm/yr average spreading rate and the zero-age center of the East Pacific Rise axis at −104.17553 E. Error on eruption distances are propagated based on interpreted age errors.

Sample	Seamount	Run ID	Interpreted Age (Ma)	Error (Ma)	Method	Ar from Inv Isochron $^{40}Ar/^{36}Ar$	$\pm^{40}Ar/^{36}Ar$	K_2O (wt %)	Lithosphere Age (Ma)	Eruption Distance (km)	Eruption Distance Error (km)	Morphology
ALV5002_14	Oscar	2718-02	**0.557**	**0.016**	Plateau	545	33	0.69	0.43	-7.10	1.76	Ridge
ALV5002_19	Oscar	2719-01	**0.584**	**0.016**	Plateau	No isochron		0.71	0.44	-7.87	1.76	Ridge
ALV4854_4	Oscar	2480-01	**0.12**	**0.077**	Inv Isochron	298.5	1.8	0.93	0.48	19.88	8.47	Coalesced
ALV4855_2	Hook Ridge	2477-01	**0.141**	**0.083**	Inv Isochron	306	12	0.80	0.64	27.30	9.13	Ridge
ALV4855_3	Hook Ridge	2733-01	**0.1746**	**0.0097**	Inv Isochron	345.4	5.9	0.98	0.64	25.50	1.07	Ridge
ALV4860_1	Beryl	2720-01	**0.233**	**0.016**	Plateau	307	14	1.19	0.96	39.79	1.76	Ridge
ALV4860_6	Beryl	2484-01	**0.084**	**0.034**	Plateau	298.4	6.4	1.51	0.98	49.03	3.74	Ridge
ALV4853_7	Beryl	2734-01	**0.204**	**0.012**	Plateau	359	12	1.20	0.98	42.93	1.32	Ridge
ALV4853_11	Beryl	2721-02	**0.2239**	**0.0079**	Plateau	311	28	1.62	1.00	42.57	0.87	Ridge
ALV4856_12	Rocky Ridge	2474-01	**0.74**	**0.43**	Inv Isochron	299.5	2.1	0.80	1.31	31.44	47.30	Coalesced
ALV4856_1	Rocky Ridge	2746-02	**1.069**	**0.043**	Plateau	311	38	0.48	1.34	15.11	4.73	Coalesced
ALV4852_3	Coral	2722-02	**0.796**	**0.022**	Plateau	490	160	0.52	1.55	41.31	2.42	Coalesced
ALV4852_5	Coral	2732-01	**0.41**	**0.29**	Inv Isochron	300.2	2.3	0.58	1.55	62.77	31.90	Coalesced
ALV4859_10	Coral	2724-02	**0.11**	**0.11**	Inv Isochron	304	5.4	0.42	1.72	88.57	12.10	Coalesced
OS14_A	Otto Ridge	2736-01	**0.572**	**0.011**	Plateau	328	19	0.81	1.89	72.56	1.21	Coalesced
ALV4857_3	Otto Ridge	2725-02	**0.84**	**0.027**	Plateau	550	220	0.56	1.93	59.68	2.97	Coalesced
ALV4858_13	Sparky	2742-01	**0.44**	**0.012**	Plateau	370	83	1.36	2.09	90.98	1.32	Ridge
ALV4858_9	Sparky	2726-02	**0.459**	**0.018**	Plateau	375	73	1.38	2.09	89.98	1.98	Ridge
ALV4858_3	Sparky	2730-02	**0.472**	**0.03**	Plateau	300	190	0.98	2.10	89.35	3.30	Ridge
OS5_D	Avery	2476-01	**1.04**	**0.32**	Inv Isochron	298.7	3.3	0.66	2.24	66.18	35.20	Seamount
OS6_D	Avery	2743-01	**2.263**	**0.026**	Inv Isochron	297.8	6.9	0.69	2.24	-1.16	2.86	Seamount
ALV4851_13	Avery	2482-01	**1.03**	**0.92**	Plateau	No isochron		0.30	2.28	68.91	101.20	Seamount
OS4_E	Avery	2744-02	**1**	**0.2**	Plateau	301.3	1.3	0.58	2.30	71.24	22.00	Seamount
ALV4850_8	Matthew	2478-01	**1.19**	**0.17**	Plateau	No isochron		0.45	2.41	66.88	18.70	Seamount
ALV4849_6	Wayne	2483-01	**1.46**	**0.56**	Inv Isochron	300.5	9	0.46	2.71	68.72	61.60	Seamount
ALV4849_14	Wayne	2745-01	**1.842**	**0.04**	Plateau	301	2	0.57	2.72	48.20	4.40	Seamount
ALV4848_14	Ivy	2481-01	**1.81**	**0.2**	Plateau	303	17	0.49	3.16	74.01	22.00	Seamount
ALV4848_5	Ivy	2731-02	**3.876**	**0.038**	Plateau	322	20	0.56	3.17	-38.88	4.18	Seamount
ALV4848_1	Ivy	2748-01	**1.55**	**0.18**	Plateau	293.3	5.8	0.67	3.18	89.49	19.80	Seamount

able from zero-age) to 3.876 +/− 0.038 Ma. However, the oldest sample (4848_5 from the most distal seamount Ivy) as well as two relatively young samples from Oscar (5002_19 and 5002_14), and one sample from Avery (OS6_D) appear to pre-date the calculated age of the underlying lithosphere on which they formed (the calculation of underlying lithosphere age is based on a 55 mm/yr spreading rate and assuming a constant zero-age locus of crustal formation at −104.17333 E on the EPR). One basalt sample from Ivy significantly pre-dates the estimated age of the lithosphere underlying it, whereas samples from Avery and Oscar have ages relatively close to the calculated crustal ages; Fig. 4). However, since the EPR neovolcanic zone likely extends ∼4 km to either side of the ridge axis (Perfit and Chadwick, 1998), and the ridge axis itself can migrate over time (Rowley et al., 2016), there is some uncertainty in our estimate for the zero-age locus of crustal formation over the past 4 Myrs. If, for example, the zero-age locus of eruptions is assumed to be −104.12709 (4 km east of its current position), the ages for Avery and Oscar samples are within error of eruption on-axis.

Calculated eruption distances (assuming a half spreading rate of 55 mm/yr) and the respective errors associated with age uncertainties are reported in Table 1 and shown in Fig. 5. Basalt eruption distances along the chain range from ∼ 0 km (essentially erupting on-axis) to ∼ 90 km, with the majority of the EMORB having erupted between 50 and 90 km from the ridge axis (Fig. 6). Eruption distances compared to underlying lithosphere ages confirm that magmatism and volcanism has occurred off-axis along the 8°20' N seamount chain (Fig. 5). In a few cases, individual seamounts erupted lavas over a wide range of distances from the ridge. For example, lavas south of Avery erupted at the ridge whereas lavas on the summit of the main round edifice erupted 75 km from the ridge, supporting previous conclusions that these seamounts form by sampling melts from various portions of the near-ridge mantle (Anderson et al., 2021; Romano et al., 2022). EMORB from Beryl, Hook Ridge, and Oscar, located closest to the EPR, have erupted approximately where they are located today (Fig. 5).

4. Discussion

4.1 *Age Constraints on Off-Axis Eruptions and Melt Focusing*

The $^{40}Ar/^{39}Ar$ ages presented here, coupled with precise sample locations and chemical analyses, provide constraints on the spatial-temporal changes in seamount volcanism and magmatic sources, which can then be related to regional tectonic and magmatic models (e.g., Fornari et al., 1989; Pockalny et al., 1997; Hebert and Montési, 2011; Keller et al., 2017; Rochat et al., 2017). Since seamounts have erupted over extended time periods and distances off-axis, geochemical systematics of the near-ridge mantle need to be assessed relative to each lava's eruption distance rather than just eruption age. Volcanism occurring as far as ∼90 km from the ridge axis is consistent with various MOR melting models (Phipps-Morgan, 1987; Langmuir et al., 1992; Forsyth et al., 1998; Hebert and Montési, 2010; Keller et al., 2017; Anderson et al., 2021), but also requires that magmas derived from small extents of melting of enriched mantle metasomatize the near-ridge lithospheric mantle that subsequently partially melts (e.g., Pilet et al., 2005; Keller et al., 2017; Rochat et al., 2017).

Fast spreading ridges like the EPR produce high volumes of melt that focus towards the ridge axis into sub-axial magma lenses, where mixing and homogenization of melts occurs (Phipps-Morgan, 1987; Spiegelman and McKenzie, 1987; Hebert and Mon-

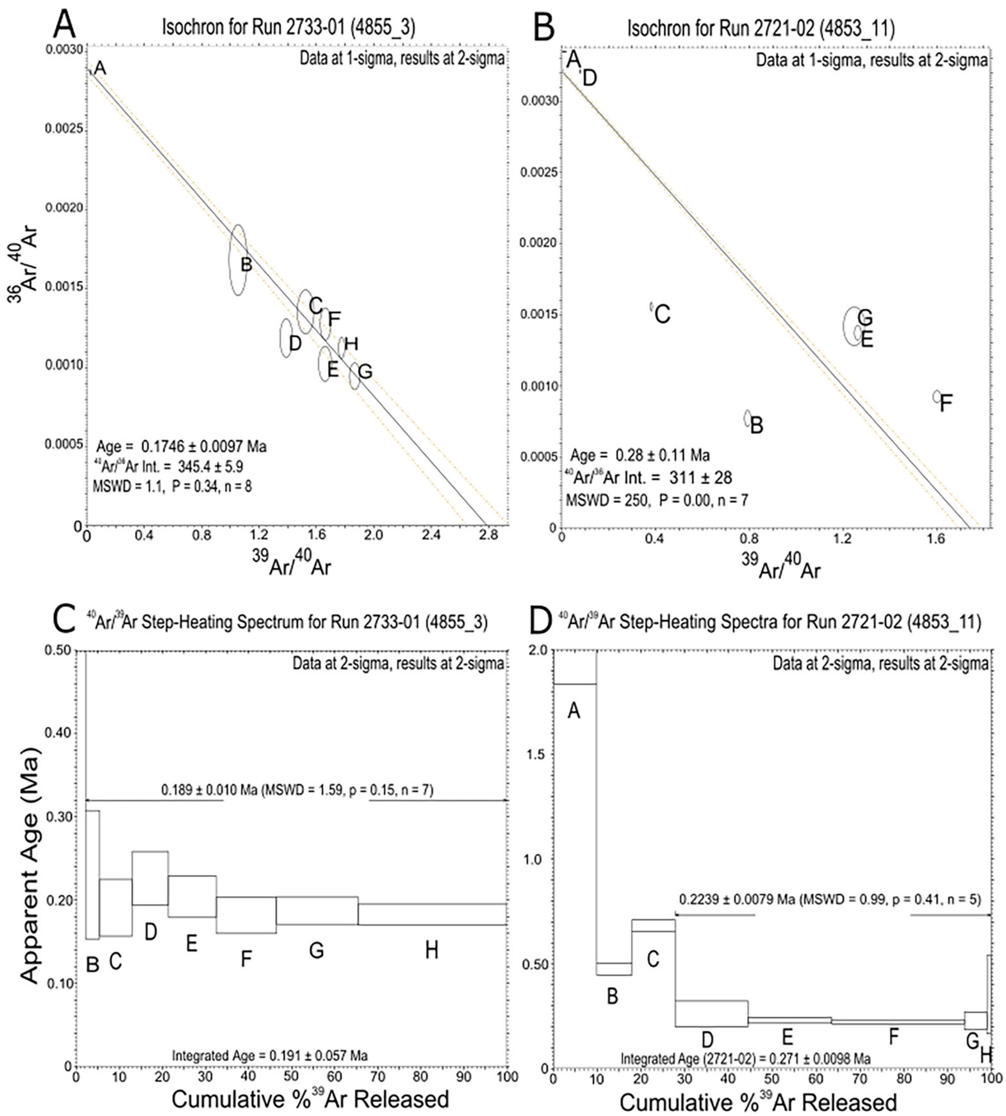

Fig. 3. A,B) $^{40}Ar/^{36}Ar$ inverse isochrons for 8°20' N seamount chain lavas 4855_3 (run 2733-01) and 4853_11 (run 2721-02) and c,d) corresponding age spectra (from Hook Ridge and Beryl respectively). Steps containing < 2% total ^{39}Ar released have been omitted from the inverse isochrons. The non-atmospheric trapped $^{40}Ar/^{36}Ar$ from 4855_3 in run 2733-01 (panel a) means that the inverse isochron age is more reliable than the plateau age, since the plateau age calculations (panel c) assume atmospheric argon and the inverse isochron does not. The inverse isochron also corresponds with the best MSWD and P-values for this sample. On the contrary, the atmospheric $^{40}Ar/^{36}Ar$ (within error) from 4853_11 in run 2721-02 and extreme MSWD and P-values for the inverse isochron (panel B) indicate that the plateau age (with best MSWD and P-values) is the more reliable age.

tési, 2010; Wanless and Shaw, 2012; Keller et al., 2017). The horizontal distance over which melt focusing results in mixing and homogenization of magmas is estimated to be about 25 km (e.g., Wanless et al., 2014; Wanless and Behn, 2017). The eruption of a large range of E- to DMORB lavas at Oscar (∼ 20 km from the EPR axis) indicates extreme heterogeneity is preserved in 8°20' N seamount melts as close as 20 km to the EPR axis (Anderson et al., 2021). Beyond the sub-axial focusing region of the EPR, geodynamic and petrologic models suggest off-axis melts migrate off-axis where they crystallize at the base of the lithosphere and metasomatize the lithospheric mantle (Niu et al., 2002; Keller et al., 2017; Rochat et al., 2017; Wanless and Behn, 2017). These models predict greater magmatic evolution of off-axis migratory melts potentially explaining why the most enriched EMORB erupting far from the EPR (those with K/Ti ratios above 30) are consistently more evolved (lower Mg-number) than the more depleted N- and DMORB lavas (Fig. 7; Anderson et al., 2021). However, without age constraints on N- and DMORB from the 8°20' N seamount chain, a systematic relationship between MORB-type melt enrichment and source variability with eruption distance is incomplete and warrants future work.

The preponderance of EMORB along the seamount chain (∼ 60% of the samples acquired) might result from a biased sampling of the youngest lavas if enriched melts preferentially formed during the latest, waning stages of volcanism on each seamount. However, eruptions of the most highly enriched EMORB between ∼50 and 90 km from the ridge axis (Fig. 7) are consistent with low extents of melting in the outer, deeper portion of the presumed triangular melt region where the asthenosphere is heterogeneously enriched and the melts have not mixed with more voluminous depleted melts closer to the EPR axis (e.g., Langmuir et al., 1992; Turner et al., 2011). Alternatively, these enriched magmas may be unrelated to a subaxial melt triangle, and instead preferentially form where the mantle is more fertile (Choi et al., 2021). In either case, enriched, low-degree melts may metasomatize the overlying lithosphere, further enriching it in incompatible elements (Pilet et al., 2011; Rochat et al., 2017).

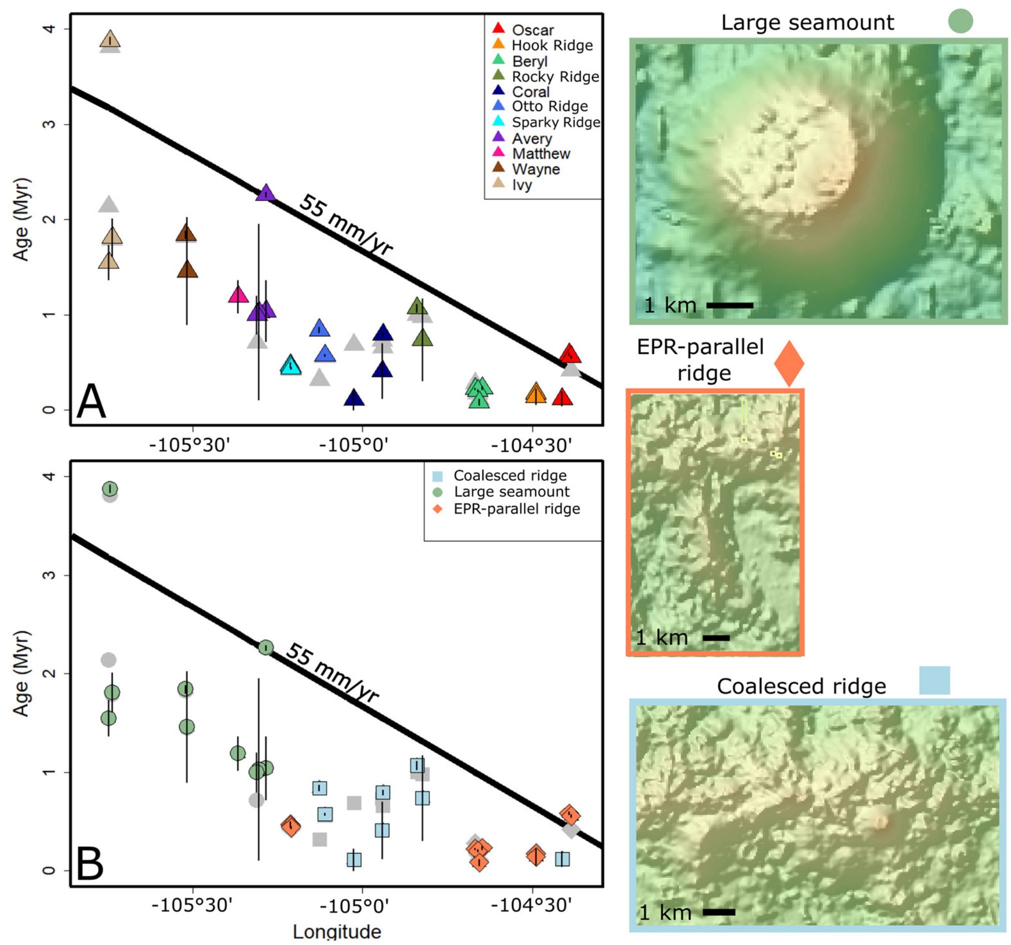

Fig. 4. Preferred $^{40}Ar/^{39}Ar$ inverse isochron and plateau ages (Myrs) for 8°20' N seamount chain lavas by A) seamount name, and B) seamount morphology, with their respective error bars compared with current longitude. Examples of each morphology type are shown on the right and color-coded with respective symbols. The center of the ridge axis is ∼ −104.17333 E. Examples of each morphology type in B are shown on the right. To demonstrate that the overall results and interpretations do not change whether the isochron or plateau age was selected, the alternative selections for each sample run (where available) are shown as grey symbols corresponding to the selected colored samples. The thick black lines represent locations where lavas should plot if they erupted at the EPR axis before the seamounts moved westward on the Pacific plate, calculated assuming a constant spreading rate of 55 mm/yr (DeMets et al., 2010). Three lavas appear to have erupted at the ridge axis but are up to 1.5 Myrs younger than the underlying lithosphere on which they erupted. Seamount lava ages range from 0 to 4 Myrs. One Ivy seamount sample (farthest from the ridge axis) is notably older than the age predicted for its underlying lithosphere. Assuming a constant half spreading rate of 55 mm/yr, the lithosphere at the Ivy sample 4848_5 location should be approximately 3.17 Ma, but the $^{40}Ar/^{39}Ar$ age of the seamount lava indicates it is 0.7 Myrs older than that estimate, at 3.88 +/− 0.04. To assess this discrepancy, this sample was prepared, irradiated, and analyzed a second time (Run ID 2885-01), reproducing a nearly identical age of 3.98 +/− 0.10 Ma. Also, inverse isochrons indicate trapped $^{40}Ar/^{36}Ar$ values above that of the atmosphere, at 322 ± 20 (original run) and 305.9 ± 6.8 (re-run; nearly atmospheric). The trapped argon artificially yields older apparent plateau ages, but this difference is only 0.066 Ma, with inverse isochron ages of 3.81 ± 0.15 (original) and 4.05 ± 0.42 (re-run). Thus, elevated initial $^{40}Ar/^{36}Ar$ does not account for the anomalously old age.

Calculated paleo-eruption locations show that EMORB with highly variable incompatible element and radiogenic isotope ratios have, in many cases, erupted at the same distance from the EPR but at different times (Fig. 7). For example, all analyzed Beryl EMORB erupted approximately 40 km from the ridge axis possess much higher incompatible element enrichments (i.e., K/Ti, $[La/Sm]_N$) and generally more radiogenic isotope ratios than the Wayne and Coral lavas that erupted the same distance from the ridge (Fig. 7). Eruptions of chemically-diverse lavas over time at given distances from the ridge axis indicates that the magmatism (e.g., melt source and melting extent) is highly dynamic over relatively short time periods (∼ Myr timescales) and spatially.

4.2 *Plate Reorganizations Responsible for 8°20' N Seamount Chain Segmentation*

During the formation of the 8°20' N seamount chain (over the past ∼ 3.6 Ma) and concurrent development of intra-transform spreading centers (ITSCs) within the Siqueiros transform, N-S trending ridges have propagated westward as the transform migrated to the south (Pockalny et al., 1997; Gregg et al., 2009; Romano et al., 2022). Fossil ITSCs that rafted away from the active transform zone are currently preserved south of the 8°20' N seamount chain along the western Siqueiros fracture zone, and may be capable of channeling melts toward the chain (Fig. 1; Supplementary Figure 1). Volcanic edifice morphologies, abyssal hill structures, and segment orientations dramatically change along the 8°20' N seamount chain forming four morphotectonic segments described earlier (Figs. 1–2). These differences are contextualized below using $^{40}Ar/^{39}Ar$ ages, to tie the evolution of the seamount chain with major regional tectonic changes associated with the Siqueiros transform fault.

The western region (WR) seamounts currently located between 150 and 175 km from the ridge axis are spatially separated and thus have not erupted continuously to coalesce into linear E-W trending ridge-like features like some of the edifices in the eastern portion of the chain. All lava ages from this region are greater than one million years, and – except for one old lava from the WCR—the WR are the oldest lavas in the entire chain, thus confirming these seamounts reflect early stages of the 8°20' N seamount chain's development. With rare exceptions, the WR lava eruption ages are consistent with the 55 mm/yr spreading rate and generally erupted

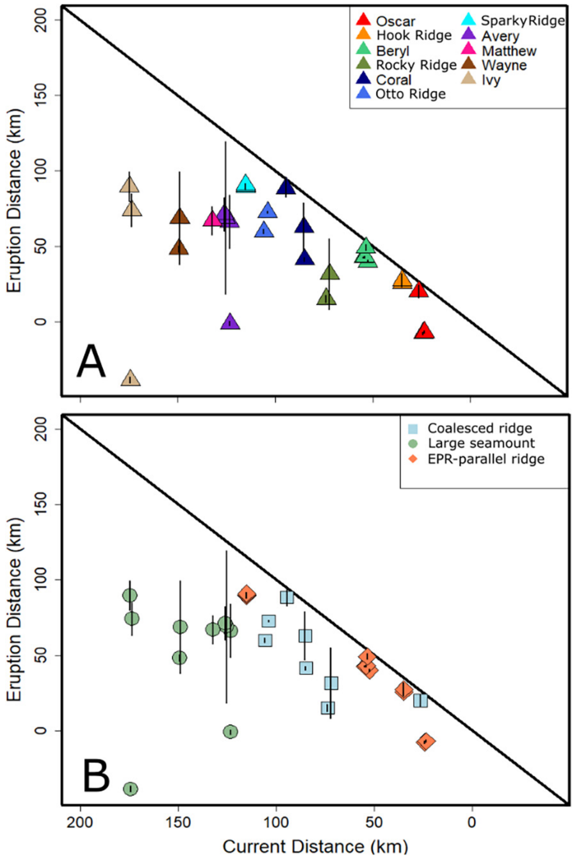

Fig. 5. Current distances from the EPR ridge axis versus calculated eruption distances of dated samples (with their respective error bars) along the span of the 8°20′ N seamount chain in terms of A) seamount name and B) seamount morphology. The 1:1 line represents loci of samples if they erupted where they are currently located. All of the EPR-parallel ridge samples plot close to this line indicating recent *in situ* formation, whereas other samples further below the line and with much greater scatter are consistent with off-axis formation and more prolonged volcanic histories.

approximately 75 km from the paleo-EPR axis (Fig. 4). This suggests that in the early stages of seamount chain development, individual seamounts grew sequentially. In turn, this implies that early off-axis EMORB magmatism occurred at a consistent and limited distance from the EPR axis. These wide ranges of measured ages, coupled with multiple lava types indicates prolonged off-axis magmatism formed the large seamounts (Supplementary Figure 2). At ∼3.9 Ma, when Ivy seamount began forming, the Siqueiros transform reorientation had initiated but had not yet abandoned any ITSCs and therefore had no apparent impact on early seamount development. Consequently, off-axis magmatism during the formation of the WR may have resembled the regional 'status quo' of punctuated, off-axis seamount generation overprinting normal N-S trending abyssal hill fabric, whereby individual seamounts grew over long periods of time.

Unlike the WR, the rest of the seamount chain has developed primarily into coalesced seamounts that form a large-scale E-W trend (Fig. 1). The western central region (WCR) currently between 100 and 150 km from the axis consists of large, sub-rounded, partially coalesced edifices as well as one sampled N-S trending, EPR-parallel ridge (Sparky Ridge). The longest-lived magmatism has formed the partially coalesced, large, and old seamount Avery and the coalesced Otto Ridge; by comparison, the EPR-parallel Sparky Ridge is significantly younger and shorter-lived (Fig. 4). Likewise, the eastern central region (ECR) currently between 60 and 100 km from the EPR axis forms a ∼40 km-long lineament of coalesced seamounts. Around the time of ECR EMORB eruptions (∼1.5 Ma), the transform had rotated a total of ∼3°. By this time, a new ITSC opened in the Siqueiros, and the original ITSCs had rafted west to ∼ −104.75° E, ∼15 km south of where Coral and Rocky Ridge are today.

Active ITSCs like those within the Siqueiros transform have been associated with a hotter mantle source and thinner crust in their fracture zones relative to typical transform faults (Gregg et al., 2006; Putirka et al., 2011). As the active zones of deformation and spreading move orthogonally away from the ridge axis, the resulting fractures can facilitate a secondary stage of magmatism (Guo et al., 2023). While magmas produced in the sub-ridge mantle may focus along a permeability boundary toward the transform fault (Hebert and Montési, 2011), it is unclear what percent of those melts instead migrate along the base of the lithosphere and produce off-axis magmatism, especially beneath the now-fossilized ITSCs and N-S trending transverse ridges. The rafting of the ITSCs and transverse ridges at ∼1.5 Ma could have provided off-axis lithospheric zones of thinning and therefore structural weakness (Behn et al., 2002; Grevemeyer et al., 2021) which would be enhanced by plate rotation and propagation of fracture zones off-axis. It is therefore possible that a migratory transform and resultant faulted lithosphere may provide zones of weakness for promoting increased melt channelization. This could result in off-axis pathways for melts feeding the chain starting approximately where Coral seamount is located today ∼100 km from the axis, where abyssal hill fabrics suddenly change to more curved and constructional morphologies (Fig. 2).

The eastern region (ER) between 20 and 60 km from the ridge axis is also characterized by a long stretch of coalesced seamounts, reflecting further channelized magmatism resulting from the tectonic reorganization occurring in the Siqueiros transform. By ∼0.5 Ma, the Siqueiros transform had rotated ∼5° counterclockwise and opened numerous ITSCs including new active ITSCs within the transform and fossil spreading sites in the fracture zone south of the chain. The ER coalesced seamount ridges are generally shorter lived than in western regions, likely because they are younger and still actively forming. For example, Oscar seamount EMORB lavas nearest the East Pacific Rise axis span only 0.4 Ma (0.58 +/− 0.02 – 0.12 +/− 0.08 Ma). The youngest segment (ER) is also characterized by abundant N-S trending hook-shaped ridges that extend southward into curvilinear abyssal hill fabric, another signal of continued, progressive changes in magmatic dynamics after the fossil ITSCs rafted away from the Siqueiros transform region between 1.5 Ma and the present day. An increase in crustal thickness over time, as inferred from gravity measurements, further supports this model for increased magmatism most recently in the seamount chain's development (Romano et al., 2022).

4.1. Origin and geochemistry of young hook-shaped ridges

The geochemical variability observed in lavas from diverse volcanic constructional morphologies further signals changes in the magmatic 'environment' associated with evolving tectonism near the Siqueiros transform. The coalesced seamounts and large seamounts in these regions consist of all three MORB types, but cones are restricted to DMORB and EPR-parallel ridges (those aligned with EPR abyssal hill fabric) are only comprised of the most enriched EMORB (Supplementary Figure 2). The $^{40}Ar/^{39}Ar$ ages of lavas from the young, EPR-parallel ridges are consistent with recent syn-tectonic formation with abyssal hills. The hook-shaped EPR-parallel ridges (i.e., Sparky Ridge, Beryl, Hook Ridge, and the southern flank of Oscar) are comprised of the youngest dated lavas from the entire chain (Fig. 4), reflecting most recent near-ridge melting conditions associated with stress regime changes in the latest stages of the opening of the transform fault.

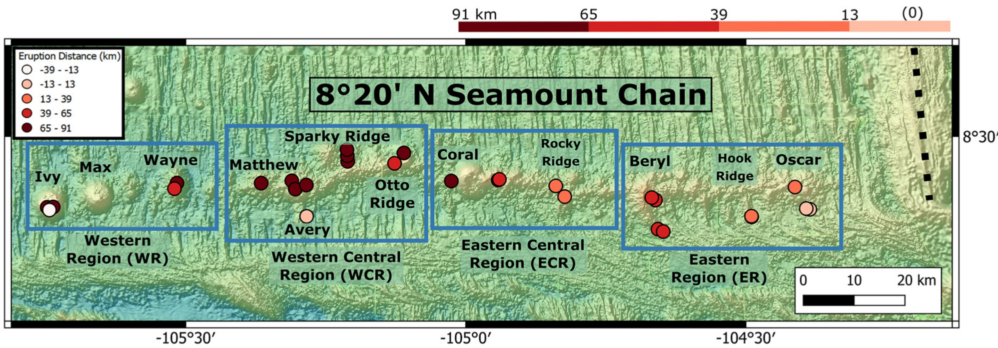

Fig. 6. EM122 bathymetry of the 8°20' N seamount chain (more details in Fig. 1) with locations of samples used for argon dating (circles). The circles are colored by eruption distance, where lighter colors correspond to lavas erupted near the East Pacific Rise (EPR) axis and darker colors correspond to lavas erupted farther from the EPR axis. Corresponding eruption distances are shown as color-coded bars above the map. The EPR axis is represented by a dashed black line. Blue boxes outline western region (WR), western central region (WCR), eastern central region (ECR), and eastern region (ER). The N-S trending EPR-parallel ridge features consistently have erupted away from the EPR axis and produce the most incompatible element enriched, and isotopically enriched lavas of the entire chain.

These young hook-shaped ridges comprise the most incompatible element-enriched lavas of the chain and of the northern EPR off-axis region (e.g., K/Ti up to 61; $[La/Sm]_N \geq 2$; Fig. 7; Supplementary Figure 3), and therefore are likely sourced from portions of the mantle distinct from other seamount lavas. The EPR-parallel ridge lavas are also more evolved than other lavas across the seamount chain (Fig. 7). Numerical models combined with observations of metasomatic enrichment in abyssal hill peridotites, ophiolites, and petit-spot garnet xenocrysts suggest that low-degree, metasomatic melts forming distal to the ridge are trapped at the base of the lithosphere (Seyler et al., 2001; Müntener et al., 2004; Keller et al., 2017; Rochat et al., 2017). The incompatible element enrichments in lavas from the hook-shaped ridges are consistent with low-degree melts migrating off-axis and metasomatizing the surrounding lithosphere, evolving and further enriching the near-ridge mantle in incompatible trace elements (Langmuir and Bender, 1984; Niu, 1997; Niu et al., 2002; Pilet et al., 2005; Keller et al., 2017; Wanless and Behn, 2017). In this manner, the enriched melts forming at the edges of the sub-ridge melting region undergo extraction off-axis that is distinct from the channelization of melts forming more proximal to the ridge.

5. Conclusions

$^{40}Ar/^{39}Ar$ ages have proven reliable for determining temporal and spatial systematics of off-axis magmatism in the incompatible element-enriched environment of the near-ridge 8°20' N seamount chain. Seamount EMORB eruptions are up to ~1.6 million years younger than their underlying MOR-generated lithosphere, supporting a model for seamount formation by off-axis magmatism that has been active at distances up to 90 km from the current ridge axis. Increasing geochemical heterogeneity with eruption distance reflects the diminishing effects of sub-ridge melt focusing. The oldest seamount lavas generally erupted approximately 75 km from the paleo-EPR axis, indicating early off-axis EMORB magmatism occurred at a consistent and limited distance from the EPR axis. Large, circular seamounts and coalesced E-W trending ridges building the bulk of the seamount chain are characterized by wide-ranging eruption ages and geochemical heterogeneity. By contrast, the most incompatible element-enriched lavas that comprise EPR-parallel ridge features within the seamount chain are the youngest constructs relative to surrounding seamounts and are largely limited to EMORB compositions. Magmas erupted from the same portions of the melt region produce suites of lavas with very heterogeneous compositions over time, suggesting the magmatic environment is dynamic over ~Myr timescales. The oldest EMORB measured erupted ~3.8 Ma, coincident with the early stages of prolonged propagation and southward migration of the Siqueiros transform fault. The coalesced ridges are hypothesized to form because of off-axis melting and melt channelization associated with zones of weakness imparted by tectonics associated with the flanking Siqueiros transform over time.

CRediT authorship contribution statement

Molly K. Anderson: Writing – review & editing, Writing – original draft, Visualization, Methodology, Investigation, Funding acquisition, Formal analysis, Data curation, Conceptualization. **Michael R. Perfit:** Writing – review & editing, Supervision, Project administration, Methodology, Investigation, Funding acquisition, Data curation, Conceptualization. **Leah E. Morgan:** Writing – review & editing, Visualization, Methodology, Formal analysis, Data curation. **Daniel J. Fornari:** Writing – review & editing, Investigation, Conceptualization. **Michael Cosca:** Writing – review & editing, Methodology, Formal analysis, Conceptualization. **V. Dorsey Wanless:** Writing – review & editing, Investigation, Funding acquisition, Conceptualization.

Declaration of competing interest

The authors declare that they have no known competing financial interests or personal relationships that could have appeared to influence the work reported in this paper.

Data availability

$^{40}Ar/^{39}Ar$ ages used in this study can be found at https://doi.org/10.5066/P9ECGKYO (Morgan, 2023). Major and trace elements and radiogenic isotope ratios in support of this manuscript are available online at EarthChem https://doi.org/10.26022/IEDA/111616 (Anderson et al., 2021).

Acknowledgements

The authors thank Laurence Coogan for the expeditious handling of this manuscript, and Ian Ridley (USGS), Charles Langmuir, and Sebastien Pilet for their very thorough reviews which significantly improved the manuscript. The authors are grateful to the captain and crew of the R/V Atlantis (AT37-05 and AT42-06), pilots of HOV Alvin and the whole AUV Sentry support team who were key to our successful field operations. They are also thankful to other members of the OASIS I and II (Off-Axis Seamount Investigation at Siqueiros) Expedition Science Teams that included Principal Investigator P. Gregg, and members M. Smith, D. Geist,

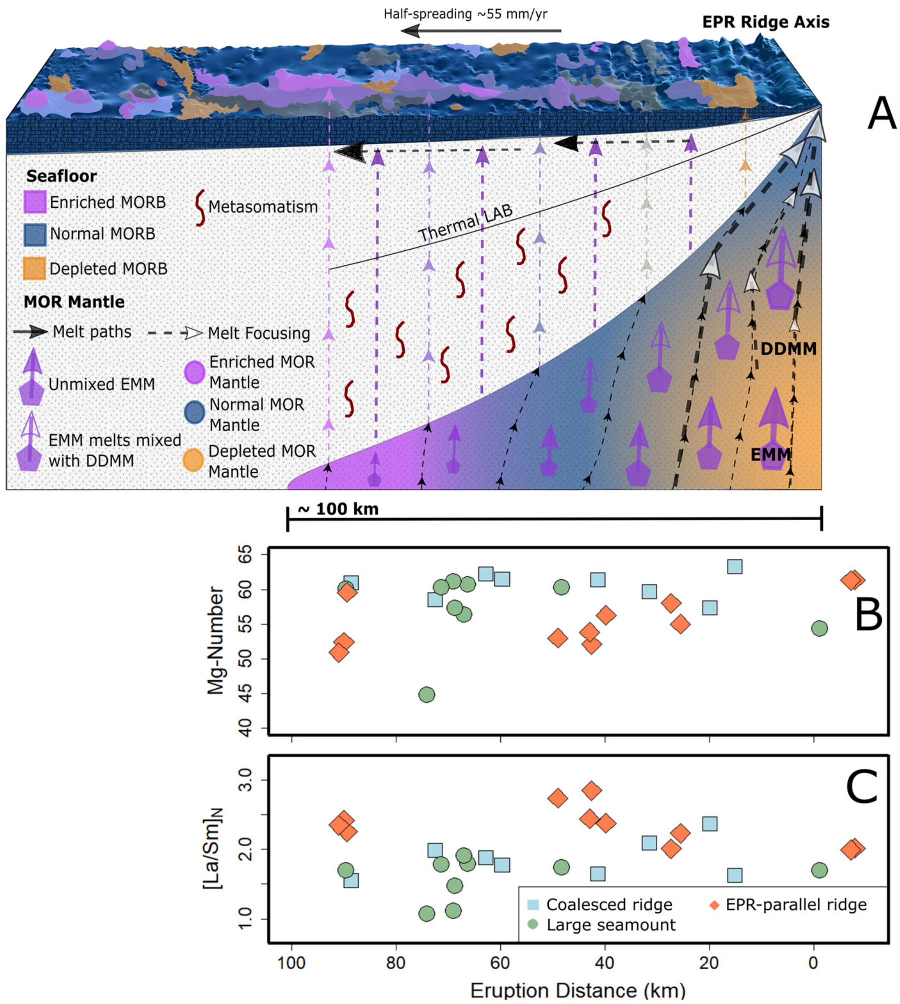

Fig. 7. A) Conceptual model of seamount formation for melting a heterogeneous mantle (modified from Anderson et al. (2021) and Keller et al. (2017)). Colors of the seafloor bathymetry of the chain of seamounts on the surface reflect compositions found along the seamounts (EMORB are enriched mid-ocean ridge basalts, NMORB are normal mid-ocean ridge basalts, and DMORB are depleted mid-ocean ridge basalts). The triangle on the lower right side beneath the ridge and seamounts represents the region of mantle melting on a single side of the ridge. The DDMM (depleted-depleted mid-ocean ridge mantle) component is represented by the continuum of purple, blue, and orange background colors which reflect the compositions of mantle melts based on degrees of melting (purple are low-degree, blue are intermediate-degree, and orange are high-degree melts) as a function of the height of the triangle. The EMM (enriched mid-ocean ridge mantle) component is superimposed as purple pentagons whose melts are the purple arrows. The filled arrows represent initial melts of EMM that have not mixed with DDMM. The open purple arrows represent EMM melts that have likely mixed with DDMM, obscuring their enriched signature (i.e., directly beneath the axis these signatures are lost to mixing and high degrees of melting; Anderson et al. (2021)). Theoretical melt paths are shown as arrows with dashed lines, indicating that some melts rise through the melt triangle, reach the top of the melt region and focus toward the ridge (within ∼20 km of the ridge), while others (particularly enriched melts) beyond the focusing region ascend vertically to the lithosphere-asthenosphere boundary where they may metasomatize the lithospheric mantle (shown in red). B) Mg-Number (Mg/Mg+Fe), C) trace element ($[La/Sm]_N$ normalized to primitive mantle (Sun and McDonough, 1989)) variations of the 8°20′ N seamount chain lavas with eruption distances (km from the ridge axis) colored by morphology. Typical precision for each ratio is within the size of the symbols. The incompatible elemental ratios and Mg-Numbers of samples are more homogeneous near the ridge axis (on the right) and more heterogeneous farther from the ridge axis (on the left). The East Pacific Rise-parallel ridge lavas (orange diamonds) possess higher $[La/Sm]_N$ ratios and lower Mg-Numbers than lavas from the other morphologic types. See supplemental information for plots of K/Ti and $^{87}Sr/^{86}Sr$.

S. Shirey, I. Ridley, B. John, C. Lundstrom, H. Cabaniss, B. Boulahanis, E. McCully, C. Trim, V. Romano, Y.J. Tan, J. Albright, Y. Zhan, and R. Parnell-Turner. Analytical assistance from R. Moscati, I. Ridley, M. Lytle, K. Bermudez, and G. Kamenov was invaluable and greatly appreciated. This work was supported by the National Science Foundation (NSF) OCE-MGG 1356610 (Romano and Gregg), NSF OCE-MGG 1356822 (Fornari), NSF OCE-MGG 1357150 (Perfit), NSF OCE-MGG 2001314 (Perfit and Wanless), the Lipman Research Award from Geological Society of America (Anderson), and the Graduate School Funding Fellowship at University of Florida (Anderson).

Appendix A. Supplementary material

Supplementary material related to this article can be found online at https://doi.org/10.1016/j.epsl.2023.118278.

References

Allan, J.F., Perfit, M.R., Fornari, D.J., Sack, R.O., 1989. Petrology of lavas from the Lamont seamount chain and adjacent East Pacific Rise, 10 N. J. Petrol. 30, 1245–1298. https://doi-org.lp.hscl.ufl.edu/10.1093/petrology/30.5.1245.

Anderson, M., Perfit, M.R., Graham, D., Kamenov, G., Forte, A., Johnston, G., 2022. Testing models for three-component mantle heterogeneity as recorded in compositions of lavas from the off-axis 8°20′ N. In: Seamount Chain, Honolulu, HI, Goldschmidt Annual Meeting. Geochemical Society.

Anderson, M., Wanless, V.D., Perfit, M., Conrad, E., Gregg, P., Fornari, D., Ridley, W.I., 2021. Extreme heterogeneity in mid-ocean ridge mantle revealed in lavas from the 8°20′N near-axis seamount chain. Geochem. Geophys. Geosyst. 22, 1–22. https://doi.org/10.1029/2020GC009322.

Batiza, R., Smith, T.L., Niu, Y., 1989. Geological and petrologic evolution of seamounts near the EPR based on submersible and camera study. Mar. Geophys. Res. 11, 169–236. https://doi.org/10.1007/BF00340203.

Behn, M.D., Lin, J., Zuber, M.T., 2002. Evidence for weak oceanic transform faults. Geophys. Res. Lett. 29, 1–4. https://doi.org/10.1029/2002GL015612.

Bowles, J., Gee, J.S., Kent, D.V., Perfit, M.R., Soule, S.A., Fornari, D.J., 2006. Paleointensity applications to timing and extent of eruptive activity, 9°-10°N East Pacific rise. Geochem. Geophys. Geosyst. 7, 1–32. https://doi.org/10.1029/2005GC001141.

Brandl, P.A., Beier, C., Regelous, M., Abouchami, W., Haase, K.M., Garbe-Schönberg, D., Galer, S.J.G., 2012. Volcanism on the flanks of the East Pacific rise: quantitative constraints on mantle heterogeneity and melting processes. Chem. Geol. 298–299, 41–56. https://doi.org/10.1016/j.chemgeo.2011.12.015.

Buck, W.R., 2001. Accretional curvature of lithosphere at magmatic spreading centers and the flexural support of axial highs. J. Geophys. Res. 106, 3953–3960.

Buck, W.R., Poliakov, A.N.B., 1998. Abyssal hills formed by stretching oceanic lithosphere. Nature 392, 272–275. https://doi.org/10.1038/246170a0.

Carbotte, S., Macdonald, K., 1992. East Pacific rise 8°–10°30′N: evolution of ridge segments and discontinuities from SeaMARC II and three-dimensional magnetic studies. J. Geophys. Res. 97, 6959. https://doi.org/10.1029/91JB03065.

Choi, H., Kim, S.S., Park, S.H., 2021. Magnetic constraints on off-axis seamount volcanism in the easternmost segment of the Australian-Antarctic Ridge. Geochem. Geophys. Geosyst. 22. https://doi.org/10.1029/2020GC009576.

Clague, D.A., Paduan, J.B., Duncan, R.A., Huard, J.J., Davis, A.S., Castillo, P.R., Lonsdale, P., Devogelaere, A., 2009. Five million years of compositionally diverse, episodic volcanism: construction of Davidson seamount atop an abandoned spreading center. Geochem. Geophys. Geosyst. 10, 1–17. https://doi.org/10.1029/2009GC002665.

Clague, D.A., Reynolds, J.R., Davis, A.S., 2000. Near-ridge seamount chains in the northeastern Pacific Ocean. J. Geophys. Res., Solid Earth 105 (B7), 16541–16561.

Clouard, V., Bonneville, A., 2005. Ages of seamounts, islands, and plateaus on the Pacific plate. Geol. Soc. Am., Spec. Pap. 388, 71–90. https://doi.org/10.1130/2005.2388(06).

Crane, K., 1976. The intersection of the Siqueiros Transform Fault and the East Pacific Rise. Mar. Geol. 21, 25–46. https://doi.org/10.1016/0025-3227(76)90102-X.

DeMets, C., Gordon, R.G., Argus, D.F., 2010. Geologically current plate motions. Geophys. J. Int. 181, 1–80. https://doi.org/10.1111/j.1365-246X.2009.04491.x.

Desonie, D.L., Duncan, R.A., 1990. The Cobb-Eickelberg seamount chain: hotspot volcanism with mid-ocean ridge basalt affinity. J. Geophys. Res. 95, 12697–12711. https://doi.org/10.1029/jb095ib08p12697.

Duncan, R.A., 1984. Age progressive volcanism in the new England seamounts and the opening of the central Atlantic Ocean. J. Geophys. Res. 89, 9980–9990.

Duncan, R.A., Hogan, L.G., 1994. Radiometric dating of young MORB using the 40Ar-39Ar incremental heating method. Geophys. Res. Lett. 21, 1927–1930. https://doi.org/10.1029/94GL01375.

Fabbrizzi, A., Parnell-Turner, R., Gregg, P.M., Fornari, D.J., Perfit, M.R., Wanless, V.D., Anderson, M., 2022. Relative timing of off-axis volcanism from sediment thickness estimates on the 8°20'N seamount chain, East Pacific Rise. Geochem. Geophys. Geosyst. https://doi.org/10.1029/2022GC010335.

Fornari, D.J., Gallo, D.G., Edwards, M.H., Madsen, J.A., Perfit, M.R., Shor, A.N., 1989. Structure and topography of the Siqueiros transform fault system: evidence for the development of intra-transform spreading centers. Mar. Geophys. Res. 11, 263–299. https://doi.org/10.1007/BF00282579.

Fornari, D.J., Perfit, M.R., Allan, J.F., Batiza, R., 1988a. Small-scale heterogeneities in depleted mantle sources: near-ridge seamount lava geochemistry and implications for mid-ocean-ridge magmatic processes. Nature 331, 511–513. https://doi.org/10.1038/332141a0.

Fornari, D.J., Perfit, M.R., Allan, J.F., Batiza, R., Haymon, R., Barone, A., Ryan, W.B.F., Smith, T., Simkin, T., Luckman, M.A., 1988b. Geochemical and structural studies of the Lamont seamounts: seamounts as indicators of mantle processes. Earth Planet. Sci. Lett. 89, 63–83. https://doi.org/10.1016/0012-821X(88)90033-7.

Fornari, D.J., Ryan, W.B.F., Fox, P.J., 1984. The evolution of craters and calderas on young seamounts: insights from Sea Marc I and Sea beam sonar surveys of a small seamount group near the axis of the East Pacific Rise at ∼10 N. J. Geophys. Res. 89 (B13), 11069–11083.

Forsyth, D.W., et al., 1998. Imaging the deep seismic structure beneath a mid-ocean ridge: the MELT experiment: the MELT seismic team. Science 280, 1215–1218. https://doi.org/10.1126/science.280.5367.1215.

Fox, P.J., Gallo, D.G., 1984. A tectonic model for ridge-transform-ridge plate boundaries: implications for the structure of oceanic lithosphere. Tectonophysics 104, 205–242. https://doi.org/10.1016/0040-1951(84)90124-0.

Gill, J., Michael, P., Woodcock, J., Dreyer, B., Ramos, F., Clague, D., Kela, J., Scott, S., Konrad, K., Stakes, D., 2016. Spatial and temporal scale of mantle enrichment at the Endeavour segment, Juan de Fuca Ridge. J. Petrol. 57, 863–896. https://doi.org/10.1093/petrology/egw024.

Graham, D.W., 2002. Noble gas isotope geochemistry of mid-ocean ridge and ocean island basalts: characterization of mantle source reservoirs:. Rev. Mineral. Geochem. 47. https://doi.org/10.2138/rmg.2002.47.8.

Graham, D.W., Zindler, A., Kurz, M.D., Jenkins, W.J., Batiza, R., Staudigel, H., 1988. He, Pb, Sr and Nd isotope constraints on magma genesis and mantle heterogeneity beneath young Pacific seamounts. Contrib. Mineral. Petrol. 99, 446–463. https://doi.org/10.1007/BF00371936.

Gregg, P.M., Behn, M.D., Lin, J., Grove, T.L., 2009. Melt generation, crystallization, and extraction beneath segmented oceanic transform faults. J. Geophys. Res., Solid Earth 114. https://doi.org/10.1029/2008JB006100.

Gregg, P.M., Lin, J., Smith, D.K., 2006. Segmentation of transform systems on the East Pacific Rise: implications for earthquake processes at fast-slipping oceanic transform faults. Geology 34, 289–292. https://doi.org/10.1130/G22212.1.

Grevemeyer, I., Rüpke, L.H., Morgan, J.P., Iyer, K., Devey, C.W., 2021. Extensional tectonics and two-stage crustal accretion at oceanic transform faults. Nature 591, 402–407. https://doi.org/10.1038/s41586-021-03278-9.

Guo, Z., et al., 2023. Disparate crustal thicknesses beneath oceanic transform faults and adjacent fracture zones revealed by gravity anomalies. Geology 51, 300–304. https://doi.org/10.1130/G50429.1.

Hall, L.S., Mahoney, J.J., Sinton, J.M., Duncan, R.A., 2006. Spatial and temporal distribution of a C-like asthenospheric component in the Rano Rahi Seamount Field, East Pacific Rise, 15°-19°S. Geochem. Geophys. Geosyst. 7. https://doi.org/10.1029/2005GC000994.

Heaton, D.E., Koppers, A.A.P., 2019. High-resolution 40Ar/39Ar geochronology of the Louisville seamounts IODP expedition 330 Drill sites: implications for the duration of hot spot-related volcanism and age progressions. Geochem. Geophys. Geosyst. 20, 4073–4102. https://doi.org/10.1029/2018GC007759.

Hebert, L.B., Montési, L.G.J., 2010. Generation of permeability barriers during melt extraction at mid-ocean ridges. Geochem. Geophys. Geosyst. 11, 1–17. https://doi.org/10.1029/2010GC003270.

Hebert, L.B., Montési, L.G.J., 2011. Melt extraction pathways at segmented oceanic ridges: application to the East Pacific Rise at the Siqueiros transform. Geophys. Res. Lett. 38, 1–5. https://doi.org/10.1029/2011GL047206.

Honda, M., Bernatowicz, T., Podosek, F.A., Batiza, R., Taylor, P.T., 1987. Age determinations of eastern Pacific seamounts (Henderson, 6 and 7) - implications for near-ridge and intraplate volcanism. Mar. Geol. 74, 79–84. https://doi.org/10.1016/0025-3227(87)90006-5.

Husen, A., Kamenetsky, V.S., Everard, J.L., Kamenetsky, M.B., 2016. Transition from ultra-enriched to ultra-depleted primary MORB melts in a single volcanic suite (Macquarie Island, SW Pacific): implications for mantle source, melting process and plumbing system. Geochim. Cosmochim. Acta 185, 112–128. https://doi.org/10.1016/j.gca.2016.02.031.

Jiang, Q., Jourdan, F., Olierook, H.K.H., Merle, R.E., Verati, C., Mayers, C., 2021. 40Ar/39Ar dating of basaltic rocks and the pitfalls of plagioclase alteration. Geochim. Cosmochim. Acta 314, 334–357. https://doi.org/10.1016/j.gca.2021.08.016.

Kamenetsky, V.S., Maas, R., 2002. Mantle-melt evolution (dynamic source) in the origin of a single MORB suite: a perspective from magnesian glasses of Macquarie Island. J. Petrol. 43, 1909–1922.

Keller, T., Katz, R.F., Hirschmann, M.M., 2017. Volatiles beneath mid-ocean ridges: deep melting, channelised transport, focusing, and metasomatism. Earth Planet. Sci. Lett. 464, 55–68. https://doi.org/10.1016/j.epsl.2017.02.006.

Koppers, A.A.P., Duncan, R.A., Steinberger, B., 2004. Implications of a nonlinear 40Ar/39Ar age progression along the Louisville seamount trail for models of fixed and moving hot spots. Geochem. Geophys. Geosyst. 5. https://doi.org/10.1029/2003GC000671.

Koppers, A.A.P., Phipps Morgan, J., Morgan, J.W., Staudigel, H., 2001. Testing the fixed hotspot hypothesis using 40 Ar/39 Ar age progressions along seamount trails. Earth Planet. Sci. Lett. 185, 237–252. http://www.elsevier.nl/locate/epsl.

Koppers, A.A.P., Staudigel, H., Duncan, R.A., 2003. High-resolution 40Ar/39Ar dating of the oldest oceanic basement basalts in the western Pacific basin. Geochem. Geophys. Geosyst. 4. https://doi.org/10.1029/2003GC000574.

Koppers, A.A.P., Staudigel, H., Wijbrans, J.R., 2000. Dating crystalline groundmass separates of altered Cretaceous seamount basalts by the 40Ar/39Ar incremental heating technique. Chem. Geol. 166, 139–158. https://doi.org/10.1016/S0009-2541(99)00188-6.

Kuiper, K.F., Deino, A., Hilgen, F.J., Krijgsman, W., Renne, P.R., Wijbrans, J.R., 2008. Synchronizing rock clocks of earth history. Science 320, 500–504. https://doi.org/10.1126/science.1154339.

Langmuir, C.H., Bender, J.F., 1984. The geochemistry of oceanic basalts in the vicinity of transform faults: observations and implications. Earth Planet. Sci. Lett. 69, 107–127. https://doi.org/10.1016/0012-821X(84)90077-3.

Langmuir, C.H., Bender, J.F., Batiza, R., 1986. Petrological and tectonic segmentation of the East Pacific Rise, 5 30' - 14 30' N. Nature 322, 422–429.

Langmuir, C.H., Klein, E.M., Plank, T., 1992. Petrological Systematics of Mid-Ocean Ridge Basalts: Constraints on Melt Generation Beneath Ocean Ridges. Geophysical Monograph Series, vol. 71, pp. 183–280.

Lee, J.Y., Marti, K., Severinghaus, J.P., Kawamura, K., Yoo, H.S., Lee, J.B., Kim, J.S., 2006. A redetermination of the isotopic abundances of atmospheric Ar. Geochim. Cosmochim. Acta 70, 4507–4512. https://doi.org/10.1016/j.gca.2006.06.1563.

Macdonald, K.C., et al., 1992. The East Pacific Rise and its flanks 8-18° N: history of segmentation, propagation and spreading direction based on SeaMARC II and Sea Beam studies. Mar. Geophys. Res. 14, 299–344. https://doi.org/10.1007/BF01203621.

Macdonald, K.C., Fox, P.J., Alexander, R.T., Pockalny, R., Gente, P., 1996. Volcanic growth faults and the origin of Pacific abyssal hills. Nature 380, 125–129.

Mallick, S., Salters, V.J., Langmuir, C.H., 2019. Geochemical variability along the northern East Pacific Rise: coincident source composition and ridge segmentation. Geochem. Geophys. Geosyst. 20 (4), 1889–1911.

Morgan, L.E., 2023. Argon data for enriched MORB from the 8°20' N seamount chain. U.S. Geological Survey data release. https://doi.org/10.5066/P9ECGKYO.

Morgan, L.E., Renne, P.R., Taylor, R.E., WoldeGabriel, G., 2009. Archaeological age constraints from extrusion ages of obsidian: examples from the Middle Awash, Ethiopia. Quat. Geochronol. 4, 193–203. https://doi.org/10.1016/j.quageo.2009.01.001.

Müntener, O., Pettke, T., Desmurs, L., Meier, M., Schaltegger, U., 2004. Refertilization of mantle peridotite in embryonic ocean basins: trace element and Nd isotopic evidence and implications for crust-mantle relationships. Earth Planet. Sci. Lett. 221 (1–4), 293–308. https://doi.org/10.1016/S0012-821X(04)00073-1.

Niu, Y., 1997. Mantle melting and melt extraction processes beneath ocean ridges: evidence from abyssal peridotites. J. Petrol. 38 (8), 1047–1074. https://doi.org/10.1093/petroj/38.8.1047.

Niu, Y., Batiza, R., 1997. Extreme mantle source heterogeneities beneath the northern East Pacific Rise: trace element evidence from near-ridge seamounts. In: International Geological Congress, 30th, Proceedings, v. 15, pp. 109–120.

Niu, Y., Regelous, M., Wendt, I.J., Batiza, R., O'Hara, M.J., 2002. Geochemistry of near-EPR seamounts: importance of source vs. process and the origin of enriched mantle component. Earth Planet. Sci. Lett. 199, 327–345. https://doi.org/10.1016/S0012-821X(02)00591-5.

Perfit, M.R., et al., 1996. Recent volcanism in the Siqueiros transform fault: picritic basalts and implications for MORB magma genesis. Earth Planet. Sci. Lett. 141, 91–108. https://doi.org/10.1016/0012-821X(96)00052-0.

Perfit, M., Chadwick, W., 1998. Magmatism at Mid-Ocean Ridges: Constraints from Volcanological and Geochemical Investigations. Geophysical Monograph Series, vol. 106, pp. 59–115.

Phipps-Morgan, J., 1987. Melt migration beneath mid-ocean spreading centers. Geophys. Res. Lett. 14, 1238–1241.

Phipps-Morgan, J., Parmentier, E.M., 1984. Lithospheric stress near a ridge-transform intersection. Geophys. Res. Lett. 11, 113–116.

Pilet, S., Baker, M.B., Müntener, O., Stolper, E.M., 2011. Monte Carlo simulations of metasomatic enrichment in the lithosphere and implications for the source of alkaline basalts. J. Petrol. 52, 1415–1442. https://doi.org/10.1093/petrology/egr007.

Pilet, S., Hernandez, J., Sylvester, P., Poujol, M., 2005. The metasomatic alternative for ocean island basalt chemical heterogeneity. Earth Planet. Sci. Lett. 236 (1–2), 148–166. https://doi.org/10.1016/j.epsl.2005.05.004.

Pockalny, R.A., Fox, P.J., Fornari, D.J., Macdonald, K.C., Perfit, M.R., 1997. Tectonic reconstruction of the Clipperton and Siqueiros fracture zones: evidence and consequences of plate motion change for the last 3 Myr. J. Geophys. Res., Solid Earth 102, 3167–3181. https://doi.org/10.1029/96jb03391.

Putirka, K., Ryerson, F.J., Perfit, M., Ridley, W.I., 2011. Mineralogy and composition of the oceanic mantle. J. Petrol. 52 (2), 279–313. https://doi.org/10.1093/petrology/egq080.

Rochat, L., Pilet, S., Müntener, O., Duretz, T., Baumgartner, L., Abe, N., Hirano, N., 2017. Garnet xenocryst from petit-spot lavas as an indicator for off-axis mantle refertilization at intermediate spreading ridges. Geology 45 (12), 1091–1094. https://doi.org/10.1130/G39427.1.

Romano, V., Gregg, P.M., Zhan, Y., Fornari, D.J., Perfit, M.R., Wanless, D., Battaglia, M., Anderson, M., 2022. The formation of the 8°20' N seamount chain, East Pacific Rise. Mar. Geophys. Res. 43, 1–15. https://doi.org/10.1007/s11001-022-09502-z.

Rowley, D.B., Forte, A.M., Rowan, C.J., Glišović, P., Moucha, R., Grand, S.P., Simmons, N.A., 2016. Kinematics and dynamics of the East Pacific Rise linked to a stable, deep-mantle upwelling. Sci. Adv. 2 (12), 1–19. https://doi.org/10.1126/sciadv.1601107.

Rubin, K.H., MacDougall, J.D., Perfit, M.R., 1994. 210Po-210Pb dating of recent volcanic eruptions on the sea floor. Nature 368 (6474), 841–844. https://doi.org/10.1038/368841a0.

Rubin, K.H., van der Zander, I., Smith, M.C., Bergmanis, E.C., 2005. Minimum speed limit for ocean ridge magmatism from 210Pb-226Ra-230Th disequilibria. Nat. Lett. 437, 534–538.

Scheirer, D.S., Macdonald, K.C., 1995. Near-axis seamounts on the flanks of the East Pacific Rise, 8°N to 17°N. J. Geophys. Res. 100, 2239–2259. https://doi.org/10.1029/94JB02769.

Seyler, M., Toplis, M.J., Lorand, J.P., Luguet, A., Cannat, M., 2001. Clinopyroxene microtextures reveal incompletely extracted melts in abyssal peridotites. Geology 29 (2), 155–158. https://doi.org/10.1130/0091-7613(2001)029<0155:CMRIEM>2.0.CO;2.

Sims, K.W.W., et al., 2003. Aberrant youth: chemical and isotopic constraints on the origin of off-axis lavas from the East Pacific Rise, 9°-10°N. Geochem. Geophys. Geosyst. 4. https://doi.org/10.1029/2002GC000443.

Sohn, R.A., Sims, K.W.W., 2005. Bending as a mechanism for triggering off-axis volcanism on the East Pacific Rise. Geology 33, 93–96. https://doi.org/10.1130/G21116.1.

Spiegelman, M., McKenzie, D., 1987. Simple 2-D models for melt extraction at mid-ocean ridges and island arcs. Earth Planet. Sci. Lett. 83, 137–152. https://doi.org/10.1016/0012-821X(87)90057-4.

Sun, S.S., McDonough, W.F., 1989. Chemical and isotopic systematics of oceanic basalts: implications for mantle composition and processes. Geol. Soc. Spec. Publ. 42, 313–345. https://doi.org/10.1144/GSL.SP.1989.042.01.19.

Turner, S., Beier, C., Niu, Y., Cook, C., 2011. U-Th-Ra disequilibria and the extent of off-axis volcanism across the East Pacific Rise at 9°30′N, 10°30′N, and 11°20′N. Geochem. Geophys. Geosyst. 12. https://doi.org/10.1029/2010GC003403.

Wanless, V.D., Behn, M.D., 2017. Spreading rate-dependent variations in crystallization along the global mid-ocean ridge system. Geochem. Geophys. Geosyst. 18, 3016–3033.

Wanless, V.D., Behn, M.D., Shaw, A.M., Plank, T., 2014. Variations in melting dynamics and mantle compositions along the Eastern Volcanic zone of the Gakkel Ridge: insights from olivine-hosted melt inclusions. Contrib. Mineral. Petrol. 167 (5), 1–22. https://doi.org/10.1007/s00410-014-1005-7.

Wanless, V.D., Shaw, A.M., 2012. Lower crustal crystallization and melt evolution at mid-ocean ridges. Nat. Geosci. 5, 651–655. https://doi.org/10.1038/ngeo1552.

Wendt, J.I., Regelous, M., Niu, Y., Hékinian, R., Collerson, K.D., 1999. Geochemistry of lavas from the Garrett transform fault: insights into mantle heterogeneity beneath the eastern Pacific. Earth Planet. Sci. Lett. 173, 271–284. https://doi.org/10.1016/S0012-821X(99)00236-8.

Wolfson-Schwehr, M., Boettcher, M.S., 2019. Global characteristics of oceanic transform fault structure and seismicity. In: Transform Plate Boundaries and Fracture Zones. Elsevier Inc.

Zindler, A., Staudigel, H., Batiza, R., 1984. Isotope and trace element geochemistry of young Pacific seamounts: implications for the scale of upper mantle heterogeneity. Earth Planet. Sci. Lett. 70 (2), 175–195.